Highly Uniform Up-Converting Nanoparticles: Why You Should Control Your Synthesis Even More

Emilia Palo[a-c,*], Minnea Tuomisto[a-c], Iko Hyppänen[a,c], Hendrik C. Swart[d], Jorma Hölsä[d], Tero Soukka[f] and Mika Lastusaari[a,c]

[a]*University of Turku, Department of Chemistry, FI-20014 Turku, Finland*

[b]*University of Turku Graduate School (UTUGS), Doctoral Programme in Physical and Chemical Sciences, Turku, Finland*

[c]*Turku University Centre for Materials and Surfaces (MatSurf), Turku, Finland*

[d]*University of the Free State, Department of Physics, Bloemfontein ZA-9300, Republic of South Africa*

[f]*University of Turku, Department of Biochemistry, FI-20014 Turku, Finland*

*Corresponding author: email: ekharj@utu.fi

ABSTRACT

Luminescent β-$NaYF_4$:Yb^{3+},Er^{3+} (x_{Yb}: 0.17, x_{Er}: 0.03) nanomaterials were synthesized for use as labels for biomedical applications with high temperature co-precipitation synthesis in 1-octadecene and oleic acid. The effect of the synthesis conditions (e.g. argon flow, cooling and stirring rates) on the products' up-conversion luminescence intensity, particle size and morphology were studied. The factors contributing to these properties were analysed. It was observed that an efficient inert gas flow is essential to the formation of the preferred highly-luminescent hexagonal structure. Furthermore, the flow rate, together with the stirring rate, crucially affect the Er:Yb molar ratio of the products. The optimization of this ratio is essential when strong up-conversion emission is required from small particles, whereas the morphology and uniformity of the nanoparticles can be controlled with the cooling

rate. These results emphasize the importance of controlling the synthesis conditions, especially when nanoparticles need to have a specific morphology because of their use e.g. as luminescent labels in medical diagnostics.

Keywords: Nanomaterials; Up-conversion luminescence; Morphology;

1. Introduction

Up-conversion luminescence is a unique type of luminescence where low energy radiation (usually near infra-red, NIR) is converted into higher energy radiation, usually in the UV-vis range (300–700 nm) [1, 2]. Different combinations of R^{3+} ions (R: rare earth, e.g. Yb-Er or Yb-Tm) as the sensitizer and activator, respectively, in selected hosts can produce up-conversion luminescence with different colours. This phenomenon has many potential applications such as enhancement of photosynthesis [3], wavelength conversion in solar cells [4], pH and ion sensors [5-7], biomedical assays [8], and medical imaging [9]. For example, in biomedical assays and applications, up-conversion luminescence nanomaterials are a highly attractive label group because of there is no autofluorescence at the visible wavelengths where the near-infrared excited anti-Stokes shifted emission is detected. This eliminates the need for time-resolved measurements required with conventional fluorescence labels [10, 11]. NIR radiation also enables the use of challenging sample matrices such as whole blood which absorbs light strongly below 600 nm [12]. When the up-converting nanophosphors are used as luminescent labels in biomedical assays they need to be uniform and monodisperse to produce efficient and equal binding sites for the biomolecules – for this reason using spherical particles would be ideal.

The $NaYF_4$ material has been found to be among the best hosts for up-conversion luminescence [13-15]. It is reported to have three different structures (low-temperature cubic, hexagonal and high-temperature cubic) [16, 17] in which the cubic structures have only one cation site while in the hexagonal structure two [16] or three [12, 18, 19] possible sites have been reported for the rare earths. Of these structures, the hexagonal form (β-$NaRF_4$; P63/m (#176), Z: 1.5 [13, 20]) has proven to be superior for the up-conversion luminescence [21]. This is thought to be due to low phonon energy in the β-$NaYF_4$ lattice (max. 350 cm^{-1} [22]) and *ca.* 0.4 Å shorter R-R distance when compared to the cubic form which favours the energy transfer from Yb^{3+} to Yb^{3+} and Er^{3+} [16]. It is also thought that the non-centrosymmetric coordination of R^{3+} ions in the β-$NaYF_4$ enhances the luminescence promoting more the 4f-4f transitions than the centrosymmetric coordination of the R^{3+} site in the cubic α-$NaYF_4$ [13, 21]. The desired hexagonal form can be obtained by introducing necessary thermal energy into the lattice to drive the irreversible phase transition from cubic to hexagonal [23, 24]. This, however, results in significant increase in the crystalline size of the material. One-pot, single stage preparation method leads to loss of intimate control of the morphology of these materials, as well.

This work was carried out to investigate the synthesis conditions of the modified [25] high temperature co-precipitation method using 1-octadecene and oleic acid [26] (Figure 1) and how the conditions affect the particle morphology and up-conversion luminescence. It is possible to achieve the requirement of high reproducibility of the prepared materials with an automation robot [27] but it is obvious that the availability of this kind of robot in common laboratory experiments is not always an option and thus investigating the synthesis parameters is crucial. This method is used as such for the synthesis of $NaRF_4$ nanoparticles, but also its

variations are reported. These include tests of different ways of introducing rare earth ions into the synthesis and the influence of reaction temperatures [28-30]. This synthesis route is also employed in the preparation of core-shell structures [31] or other host materials such as $KMnF_3$ [32]. However, to the authors' knowledge the impact of the parameters studied in the present work have not been reported previously.

In this study it was important to produce uniformly sized nanoparticles with desired morphology – in most cases spherical - to be used as luminescent labels in biomedical assays [8, 9]. The protective inert gas flow (argon), duration of cooling period, and stirring rate during the synthesis (Figure 1) were studied for their effect on the nanomaterial properties. Moreover, as the increase in the nanoparticle size strengthens significantly up-conversion luminescence [33], an appropriate compromise between these properties was investigated.

2. Materials and methods

2.1. Materials preparation

The $NaYF_4:Yb^{3+},Er^{3+}$ nanomaterials were prepared with the synthesis procedure reported previously [25] using selected dopant concentrations (x_{Yb}: 0.17 and x_{Er}: 0.03) (Figure 1.). In the synthesis, methanol solutions (0.2 mol dm^{-3}) of RCl_3 (R: Y, Yb, Er, 6 cm^3 in total) were added to a 250 cm^3 flask containing 1-octadecene and oleic acid (21 and 9 cm^3, respectively). This solution was then heated to and maintained at 160 °C for 40 minutes and further cooled down (in 15 or 30 min) to room temperature under argon atmosphere (1-3 dm^3 h^{-1} flow).

Then, a methanol solution containing NH_4F and NaOH (0.18 and 0.12 g, respectively, in total 15 cm^3) was added into the mixture described above and stirred

for 30 minutes at room temperature (125 to 625 rpm). The solution was subsequently heated and maintained at 310 °C for 90 minutes under argon flow and again cooled down (in 15 or 30 min) to room temperature. Both cooling times were kept the same during the same synthesis. The products were eventually precipitated by the addition of ethanol and collected by centrifugation. The products were washed several times with absolute ethanol and dried at room temperature in a vacuum desiccator for characterization. When the specific parameter was not under investigation the values for argon flow rate, cooling time and stirring rate were 2 dm^3 h^{-1}, 30 min and 375 rpm, respectively.

All chemicals used were of analytical grade. Yttrium, ytterbium and erbium chloride hexahydrate ($RCl_3 \cdot 6H_2O$, 99.99 %, purity with respect to other rare earths), ammonium fluoride (NH_4F 99.99 %), sodium hydroxide (NaOH, 99.99), 1-octadecene (90) and oleic acid (90) were all purchased from Sigma-Aldrich. Absolute ethanol and methanol were used as received.

2.2. Characterization

The particle morphologies were determined with a Tecnai 12 Bio Twin transmission electron microscope equipped with a CCD camera. The acceleration voltage was 120 kV giving the resolution of 0.49 nm. Before measurements, the samples were prepared dispersing the up-converting nanomaterials into a diluted toluene and then drying a drop on the surface of a carbon coated copper grid. An average particle diameter were calculated with the ImageJ software version 1.43s [34] (http://rsb.info.nh.gov/ij) from 100 particles.

The XPD measurements were used to probe the structure and phase purity of the nanomaterials. The patterns were collected at room temperature with a Huber

G670 image plate Guinier camera (Cu $K_{\alpha 1}$ radiation, 1.5406 Å) with the 2θ range between 4 and 100° (step 0.005°). Data collection time was 30 min and 10 data reading scans of the image plate.

The crystallite sizes of the $NaYF_4:Yb^{3+},Er^{3+}$ nanomaterials were estimated also from the diffraction data using the Scherrer formula (Eq. 1) [35]. In this equation, d is the mean crystallite size (m), λ the X-ray wavelength (m), β (rad) the full width at half maximum (FWHM) of the chosen reflection and θ (°) half of the Bragg´s angle (2θ). Reflection broadening due to the diffractometer was eliminated from the β_s value by using a microcrystalline reference (β_r; Eq. 2). The commercial, microcrystalline $NaYF_4:Yb^{3+},Er^{3+}$ (PTIR 550/F, Phosphor Technology, Stevenage, England) was then used. The (002) and (200) reflections were used to calculate the thickness of the hexagonal plates and the width of the hexagonal faces, respectively, thus giving an estimate of the anisotropy of the size and morphology of the nanocrystallites.

$$d = \frac{0.9\lambda}{\beta\cos\theta} \quad (1) \qquad \beta^2 = \beta_s^2 - \beta_r^2 \quad (2)$$

The elemental compositions of the products were probed with X-ray fluorescence spectroscopy (XRF) using the PANalytical epsilon 1 apparatus using the internal Omnian calibration.

The up-conversion luminescence and its behaviour with different excitation power densities was studied with NIR laser excitation at 976 nm. This excitation is in a good resonance with the $^2F_{5/2}$ and $^4I_{11/2}$ energy levels of Yb^{3+} and Er^{3+}, respectively. This enables the efficient energy transfer up-conversion process (ETU) of the Yb^{3+}-Er^{3+} pair (Figure 2) that has been well described in the literature [1,2] but also recently revisited [36]. In the ideal situation, the process involves two

successive energy transfer steps from an excited Yb^{3+} ion ($^2F_{5/2} \rightarrow {}^2F_{7/2}$) to an Er^{3+} ion (the $^4I_{15/2} \rightarrow {}^4I_{11/2}$ and $^4I_{11/2} \rightarrow {}^4F_{7/2}$ transitions, respectively) resulting in green ($^2H_{11/2}$,$^4S_{3/2} \rightarrow {}^4I_{15/2}$, 515-560 nm) up-conversion luminescence. In addition, after a third energy transfer following with a multiphonon relaxation this complex process may result in blue ($^2H_{9/2} \rightarrow {}^4I_{15/2}$, 442 nm) or, with a back energy transfer to Yb^{3+} in red ($^4F_{9/2} \rightarrow {}^4I_{15/2}$ transitions, 640-685 nm) up-conversion luminescence from Er^{3+}. The up-conversion luminescence spectra were measured at room temperature with an Ocean Optics PC2000-CCD spectrometer. A continuous wave Hamamatsu L9418-04 NIR laser diode (λ_{exc}: 976 nm (10 200 cm^{-1}), FWHM: 4 nm (43 cm^{-1})) was used as an excitation source. The diameter of the focused laser beam spot was estimated to be 2 mm. Laser power was controlled by adjusting the operating current with a laser driver (Newport Laser Diode Driver 5060) resulting in excitation power density range 0.4 to 10.3 W cm^{-2}. Nanomaterials (dry powders) were held inside a rotating capillary tube. Before the sample an RG850 long-pass filter with a cut-off at 850 nm (Edmund Optics) was used to ensure a pure NIR excitation and after the sample an extended hot mirror filter (Edmund Optics) with a good transmission in visible was used to exclude the scattered excitation radiation. The emission was collected at a 90° angle to the excitation and directed to the spectrometer with an optical fibre (diameter 200 µm). The spectral response was calibrated with an Ocean Optics LS-1-CAL-INT calibration source.

The rise and decay curves of the green and red emissions were measured at room temperature with a modular luminometer. NI USB-6251 (National instruments) analog-to-digital converter was used to generate square-wave excitation pulse profile for the laser driver (Newport Laser Diode Driver 5060). Excitation source was a fibre coupled NIR laser diode (IFC-975-008-F) with 973 nm (10 300 cm^{-1}). The diameter of

the focused laser beam spot was estimated to be 3 mm. The optical part of the luminometer consisted of tubular excitation and emission chambers (Thorlabs, Inc., Newton, NJ) in a right-angle configuration, and a holder for sample capillary. The same long-pass filter as with the spectral measurements was used in front of the sample. After the sample a 900 nm short-pass filter (Newport 10SWF-900-B) and filters with the desired bandpass 544/10 or 650/10 nm (Thorlabs FB543.4-10 and FB650-10) were used. The detector at the end of emission chamber was a head-on R1464 photomultiplier (Hamamatsu Photonics, Hamamatsu City, Japan). The photomultiplier signal was amplified in a high-speed current amplifier DHPCA-100 (Femto Messtechnik GmbH, Germany). The amplified signal was recorded with the NI USB-6251 A/D converter connected to a computer via USB and controlled with a computer program written in LabVIEW 8.5 (National Instruments). The pulse profile used consisted of a 20 ms excitation pulse followed by a 30 ms measurement time before the next pulse. During a single measurement the pulse profile was cycled 10,000 times resulting in a measurement time of 8.3 min. In rise and decay fittings (S3-S6) two or three exponential decay components were needed to obtain reasonable fit [37].

3. Results and discussion

3.1. Controlling crystal structure and morphology

The synthesized $NaYF_4:Yb^{3+},Er^{3+}$ (x_{Yb}: 0.17, x_{Er}: 0.03) nanomaterials were characterized with X-ray powder diffraction to distinguish between the favoured hexagonal form and the undesired cubic form (α-$NaRF_4$; $Fm\bar{3}m$ (#225), Z: 2 [20]). Also the morphology of the nanomaterials was determined from the TEM images.

The cubic form was obtained in the syntheses only when using the argon flow rate of 1 dm^3 h^{-1} (Figure 1), though even then there was also a small amount of hexagonal form present (Figure 3, top). When the argon flow rate was increased, the preferred hexagonal form was obtained exclusively. This suggests that only an argon flow rate high enough can remove the evaporated methanol and HCl from the synthesis flask. The incomplete evaporation induces the formation of a NaCl impurity and thus inhibits the formation of the hexagonal structure that needs a higher excess of Na^+ than the cubic one to form [16].

By establishing an efficient argon flow the formation of the NaCl impurity could be diminished or even prevented. The TEM images (Figure 3, bottom) show that the synthesis using the argon flow of 1 dm^3 h^{-1} resulted in the formation of particles with many different sizes and varying quasi-spherical and hexagonal plate-like structures. With higher flow rates, monodisperse sets of nanoparticles that are uniform in shape and size were obtained (Table S1; Figure 3, bottom).

Because the argon flow was projected into the gas phase on top of the liquid instead of below the liquid surface, one can assume that there will be no local cooling inside the liquid phase due to the gas flow that would affect crystallization. On the other hand, the flow rate seems to play an important role in controlling the distances between the crystallite nucleation sites. High enough separation distances will ensure that as few as possible nucleation sites will be allowed to combine to yield bigger crystallites. One can assume that this effect is due to the control of the evaporation of HCl, *i.e.* the “chemical stirring” of the liquid phase.

The duration of the cooling period after the two heating stages had no significant effect on the crystal structure of the nanomaterials (Figure 4, top). However, the effect on crystallite size is significant: ca. 50×65 (hexagonal plate

diameter×thickness) and 20×30 nm for the 15 and 30 min cooling times, respectively.

As there are no crystallites present after the first cooling step, it seems that the impact on crystallite size results from the second cooling step. One would expect that a slower cooling rate would give larger crystallites because of the possible Ostwald ripening process [29], but here the opposite is observed: there were both small quasi-spherical as well as large hexagonal shaped particles present in the nanomaterial cooled down faster (Figure 4, bottom). Therefore, it seems that the first cooling is the more important one providing efficient start up for the formation of the cubic particles. During this stage, the rare earth oleates may precipitate forming colloidal solutions and also at this stage the argon (or any inert) gas flow should be sufficient in removing the by-products such as HCl so they won't interfere with the particles on later stage. It can be postulated that if the oleates form bigger particles (slow cooling), they will be less reactive than smaller particles (fast cooling), which leaves less time for the crystal growth of NaYF4:Yb,Er. Because of the narrow size distribution of the nanoparticles formed during the slower cooling it must be noted that the cooling time seems to be short enough to prevent the Ostwald ripening process that could result into wider size distribution of the nanoparticles [29].

The XPD pattern shows that the intensity ratio of the (110) and (101) reflections is different with different cooling times. As reported previously for $NaYF_4:Yb^{3+},Tb^{3+}$ [38], such difference in the reflection intensities suggests that with fast cooling the R^{3+} ions occupy predominantly the Na/R site whereas with slow cooling also the Na^+ site is partly occupied by R^{3+}. The latter case would make the distances between R^{3+} ions shorter, which would enhance energy transfer and thus affect up-conversion luminescence intensity. Depending on which R^{3+} would occupy

250 the Na^+ sites, the up-conversion emission could be strengthened or weakened,
251 however.
252 Varying the stirring rate in the synthesis did not affect the formation of the
253 hexagonal form (Figure S1, top). Though it seems that decreasing the stirring rate
254 could lead to smaller nanoparticles (Table S1), the calculated crystallite sizes range
255 between 18 and 32 nm and the variation is too small for any definite conclusions.
256 The TEM images (Figure S1, bottom) revealed that the particle morphology was
257 uniform for all nanomaterials. The particles of the nanomaterial prepared with the
258 stirring rate of 375 rpm are slightly larger than with the other rates. However, this
259 cannot be observed in the crystallite sizes calculated with the Scherrer equation
260 (Table S1).
261 When the calculated crystallite sizes and average particle diameters obtained
262 from the TEM images are compared (Table S1) it can be seen that the average
263 diameter is larger than the calculated sizes, as can be expected. However, the
264 behaviour of the size is similar in both cases.
265
266 **3.2. Beating the size effect on up-conversion luminescence intensity**
267 For the rare earth doped luminescent nanoparticles, the intensities of luminescence
268 emissions are often in interplay with the crystallite sizes. This is because the smaller
269 are the crystallites the more important will be the quenching surface effects. This will
270 then lead to decreasing emission output with decreasing crystallite size.
271 In the present work, all synthesized materials show up-conversion
272 luminescence that corresponds to that expected from an Yb^{3+}-Er^{3+} pair (Figures S2).
273 To investigate if the differences in the materials' up-conversion luminescence

intensities could be explained by other factors than crystallite size, the emission intensities were plotted against the average crystallite sizes (Figure 5).

Both the green and red up-conversion luminescence intensities show a clear dependency on the crystallite for all but three cases. Stirring of 375 rpm, cooling of 30 min and argon flow of 2 dm^3 h^{-1} result in stronger emission than expected from their crystallite sizes (Figure 5). A very similar trend is observed for the respective emission rise (Figure 6; see Figures S3-S4 for the rise curves) as well as decay times (Figures S5 and S6). The latter is in agreement with what has been reported earlier for $NaYF_4$:Yb,Er [39]. These observations indicate that the emission intensities and rise/decay times correlate in the putative way, e.g. the stronger is the emission the longer is the rise/decay time. Again, this can be explained by the surface effects: the smaller crystallites have more surface, more surface defects and thus faster processes.

For the green emission the ratio of rise and decay times shows a narrow distribution between 2.6 and 2.9 for the materials studied (Figure 7). This suggests that the factors affecting the emission kinetics influence equally both the feeding and decay of the green Er^{3+} up-conversion emission. Due to the small size of the materials it is expected that the multiphonon relaxations increased by the possible surface impurities play an important role in the decrease in the green up-conversion luminescence.

For the red emission, on the other hand, the ratio decreases from 3.1 to 2.1 with increasing red to green emission intensity ratio. Thus, the higher is the dominance of the red emission the shorter is its rise time in comparison with the respective decay time. Also here the aforementioned three materials stand out by showing the lowest rise to decay time ratios suggesting the most efficient feeding of

the red-emitting levels. Because the red emission is a product of the back energy transfer involving close by Yb^{3+} ions [36] this suggest that they are spread at the close range within Er^{3+} ions thus enabling the efficient overall up-conversion process at the same time. The material prepared using the 15 min cooling time also shows a low value for the time ratio, but this material has clearly the largest crystallites.

To find out why the three cases mentioned above have the best performance, XRF measurements were carried out. The present results suggest that there is an optimum Er/Yb ratio at *ca.* 0.35 and that the best-performing three cases have this ratio. The optimum ratio can be achieved only with optimized physical (stirring) and chemical (argon flow) mixing (Figure 8). It means that the mixing must be vigorous enough to allow a good homogenization of the Yb^{3+} and Er^{3+} species, but not so harsh that it would break the formed crystallite seeds.

3.3. Improving sensitivity for detection

When the up-conversion emission intensity is plotted as a function of the excitation power density, it can be seen that the intensity varies significantly for materials synthesized with different conditions (Figure 9). If the behaviour is assumed exponential, it is possible to estimate from these curves the threshold power density with which up-conversion can be obtained. In the present case up-conversion luminescence can be obtained even with excitation power density of 0.38 W cm^{-2} which gives good estimation that it could be achieved even with lower power densities. Moreover, the curve for the cubic nanomaterial prepared with argon flow rate of 1 dm^3 h^{-1} shows only a gradual rise with increasing power density compared to the nanomaterial prepared with a argon flow rate of 2 dm^3 h^{-1} the latter showing a steeper curve.

The curves also show that even though the nanomaterial prepared with 15 min cooling time has a higher luminescence intensity than the nanomaterial prepared with 30 min cooling time, the latter is not significantly weaker. This a very good indication that the crystallite size does not necessarily need to be significantly larger to show good up-conversion luminescence, if the Er/Yb composition is good, as discussed above.

These results show that it is possible to improve sensitivity by controlling the synthesis parameters. For the labelling techniques, it is important to obtain the detection of lower concentrations of the analytes as well as to avoid the damage caused by high excitation power.

4. Conclusions

The high temperature co-precipitation method [26] can be considered as the most widely used protocol for synthesizing up-converting $NaYF_4$ based nanoparticles suitable for luminescent biolabeling. It is common knowledge that the temperature and duration of the heating stages will have a strong effect on the outcomes of the syntheses. However, the results of the present work show that there are other – maybe often ignored – factors that also have strong influence. It turned out that controlling these factors (cooling speed, stirring rate and argon flow rate) allows the tailoring of the crystallite size, morphology, Er/Yb ratio and crystal structure of the $NaYF_4$ particles (Figure 10). These are all important feasibility features when considering the performance of the nanoparticles. Of course, it remains a choice of the researcher how to tailor the materials, for example whether smaller or bigger particles would be better for the application. The present results will offer the tools for such choices.

Acknowledgements

Financial support from the Finnish Funding Agency for Technology and Innovation (Tekes) “UPCORE” project and Nordic Energy Research “AquaFEED” project are gratefully acknowledged. Additional financial support was given to JH by the Academy of Finland – Republic of South Africa program (Project #279613). The authors would like to thank Dr. Riikka Arppe for the TEM images.

References

[1] F. Auzel, Upconversion and Anti-Stokes Processes with f and d Ions in Solids, Chem. Rev. 104 (2004) 139–173.

[2] Y. Mita, Other phosphors, in S. Shionoya, W.M. Yen (Eds.), Phosphor handbook, CRC Press: Boca Raton, FL, USA, 1999, pp. 643–650.

[3] T. Antal, E. Harju, L. Pihlgren, M. Lastusaari, T. Tyystjärvi, J. Hölsä, E. Tyystjärvi, Use of Near-Infrared Radiation for Oxygenic Photosynthesis via Photon Up-Conversion, Int. J. Hydrogen Energ. 3 (2012) 8859–8863.

[4] J. de Wild, A. Meijerink, J.K. Rath, W.G.J.H.M van Stark, R.E.I. Schropp, Upconverter Solar Cells: Materials and Applications, Energy Environ. Sci. 4 (2011) 4835–4848.

[5] R. Arppe, T. Näreoja, S. Nylund, L. Mattsson, S. Koho, J.M. Rosenholm, T. Soukka, M. Schäferling, Photon Upconversion Sensitized Nanoprobes for Sensing and Imaging of pH, Nanoscale 6 (2014) 6837−6843.

[6] J. Liu, Y. Liu, Q. Liu, C. Li, L. Sun, F. Li, Iridium(III) Complex-Coated Nanosystem for Ratiometric Upconversion Luminescence Bioimaging of Cyanide Anions, J. Am. Chem. Soc. 113 (2011) 15276–15279.

[7] Q. Liu, J. Peng, L. Sun, F. Li, High-Efficiency Upconversion Luminescent Sensing and Bioimaging of Hg(II) by Chromophoric Ruthenium Complex-Assembled Nanophosphors, ACS Nano 5 (2011) 8040–8048.

[8] R. Arppe, L. Mattsson, K. Korpi, S. Blom, Q. Wang, T. Riuttamäki, T. Soukka, Homogeneous Assay for Whole Blood Folate Using Photon Upconversion, Anal. Chem. 87 (2015) 1782–1788.

[9] M. Ylihärsilä, T. Valta, M. Karp, L. Hattara, E. Harju, J. Hölsä, P. Saviranta, M. Waris, T. Soukka, Oligonucleotide Array-in-Well Platform for Detection and Genotyping Human Adenoviruses by Utilizing Upconverting Phosphor Label Technlogy, Anal. Chem. 83 (2011) 1456–1461.

[10] T. Soukka, K. Kuningas, T. Rantanen, V. Haaslahti, T. Lövgren, Photochemical Characterization of Up-Converting Inorganic Lanthanide Phosphors as Potential Labels, J. Fluoresc. 15 (2005) 513–528.

[11] P. Diamandis, T.K. Christopoulos, Europium Chelate Labels in Time-Resolved Fluorescence Immunoassays and DNA Hybridization Assays, Anal. Chem. 62 (1990) 1449A–1157A.

[12] K. Kuningas, H. Päkkilä, T. Ukonaho, T. Rantanen, T. Lövgren, T. Soukka, Upconversion Fluorescence Enables Homogeneous Immunoassay in Whole Blood, Clin. Chem. 53 (2007) 145−146.

[13] K.W. Krämer, D. Biner, G. Frei, H.U. Güdel, M. Hehlen, S. Lüthi, Hexagonal Sodium Yttrium Fluoride Based Green and Blue Emitting Upconversion Phosphors, Chem. Mater. 16 (2004) 1244–1251.

[14] J. Zhao, Y. Sun, X. Kong, L. Tian, Y. Wang, L. Tu, J. Zhao, H. Zhang, Controlled Synthesis, Formation Mechanism, and Great Enhancement of Red

Upconversion Luminescence of $NaYF_4:Yb^{3+},Er^{3+}$ Nanocrystals/Submicroplates at Low Doping Level, J. Phys. Chem. B. 112 (2008) 15666–15672.

[15] I. Hyppänen, J. Hölsä, J. Kankare, M. Lastusaari, L. Pihlgren, T. Soukka, Preparation and Up-Conversion Luminescence Properties of $NaYF_4:Yb^{3+},Er^{3+}$ Nanomaterials, Terrae Rarae 16 (2009) 1–6.

[16] E. Harju, I. Hyppänen, J. Hölsä, J. Kankare, M. Lahtinen, M. Lastusaari, L. Pihlgren, T. Soukka, Polymorphism of $NaYF_4:Yb^{3+},Er^{3+}$ Up-Conversion Luminescence Materials, Z. Kristallogr. Proc. 1 (2011) 381–387.

[17] R.E. Thoma, H. Insley, G.M. Hebert, The Sodium Fluoride-Lanthanide Trifluoride Systems, Inorg. Chem. 5 (1966) 1222–1229.

[18] J.H. Burns, Crystal Structure of Hexagonal Sodium Neodymium Fluoride and Related Compounds, Inorg. Chem. 4 (1965) 881–886.

[19] A. Grzechnik, P. Bouvier, W.A. Crichton, L. Farina, J. Köhler, Metastable $NaYF_4$ Fluorite at High Pressures and High Temperatures, Solid State Sci. 4 (2002) 895–899.

[20] PCPDFWIN v. 1.30, Powder Diffraction File, 1997, International Centre for Diffraction Data (ICDD), entries 06-0342 (cubic $NaYF_4$) and 28-1192 (hexagonal $Na(Y_{0.57}Yb_{0.39}Er_{0.04})F_4$).

[21] J.L. Sommerdijk, On the Excitation Mechanisms of the Infrared-excited Visible Luminescence in Yb^{3+},Er^{3+} -Doped Fluorides, J. Lumin. 6 (1973) 61–67.

[22] J.F. Suyver, J. Grimm, M.K. van Veen, D. Biner, K.W. Krämer, H.U. Güdel, Upconversion Spectroscopy and Properties of $NaYF_4$ Doped with Er^{3+}, Tm^{3+} and/or Yb^{3+}, J. Lumin. 117 (2006) 1–12.

421 [23] M.D. Mathews, B.R. Ambekar, A.K. Tyagi, J. Köhler, High Temperature X-ray
422 Diffraction Studies on Sodium Yttrium Fluoride, J. Alloys Compd. 377 (2004)
423 162–166.
424 [24] T. Laihinen, M. Lastusaari, L. Pihlgren, L.C.V. Rodrigues, J. Hölsä, Thermal
425 Behavior of the $NaYF_4$:Yb^{3+},R^{3+} Materials, J. Therm. Anal. Calorim. 121 (2015)
426 37–43.
427 [25] M. Ylihärsilä, E. Harju, R. Arppe, L. Hattara, J. Hölsä, P. Saviranta, T. Soukka,
428 M. Waris, Genotyping of Clinically Relevant Human Adenoviruses by Array-in-
429 well Hybridization Assay, Clin. Microbiol. Infect. 19 (2013) 551–557.
430 [26] F. Wang, Y. Han, C.S. Lim, Y. Lu, J. Wang, J. Xu, H. Chen, C. Zhang, M. Hong,
431 X. Liu, Simultaneous Phase and Size Control of Upconversion Nanocrystals
432 Through Lanthanide Doping, Nature 463 (2010) 1061–1065.
433 [27] E.M. Chan, G. Han, J.D. Goldberg, D.J. Gargas, A.D. Ostrowski, P.J. Schuck,
434 B.E. Cohen and D.J. Milliron, Combinatorial Discovery of Lanthanide-Doped
435 Nanocrystals with Spectrally Pure Upconverted Emission, Nano Lett. 12 (2012)
436 3839–3845.
437 [28] A. Bednarkiewicz, D. Wawrzynczyk, M. Nyk, M. Samoc, Tuning Red-Green-
438 White Up-Conversion Color In Nano $NaYF_4$:Er/Yb Phosphor, J. Rare Earth. 29
439 (2011) 1152–1156.
440 [29] T. Rinkel, J. Nordmann, A.N. Raj, M. Haase, Ostwald-ripening and Particle Size
441 Focussing of sub-10 nm $NaYF_4$ Upconversion Nanocrystals, Nanoscale 6
442 (2014) 14523–14530.
443 [30] N.J.J. Johnson, C.J.M. van Veggel, Lanthanide-Based Heteroepitaxial Core-
444 Shell Nanostructures: Compressive Versus Tensile Strain Asymmetry, ACS
445 Nano 8 (2014) 10517–10527.

[31] X. Wu, S. Hu, C. Tan, Y. Liu, Simultaneously Optimizing Fluorescent and Paramagnetic Properties of Bifunctional $NaGdF_4:Yb^{3+}/Er^{3+}$ Nanocrystals by Crystal Field Tuning, Mater. Res. Bull. 64 (2015) 22–26.

[32] H. Wang, X. Hong, R. Han, J. Shi, Z. Liu, S. Liu, Y. Wang, Y. Gan, Triple-doped $KMnF_3:Yb^{3+}/Er^{3+}/Tm^{3+}$ Nanocubes: Four-color Upconversion Emissions with Strong Red and Near-infrared Bands, Sci. Rep. 5 (2015) Article number 17088.

[33] M. Ding, S. Yin, Y. Ni, C. Lu, D. Chen, J. Zhong, Z. Ji, X. Zhongzi, Controlled Synthesis of β-$NaYF_4:Yb^{3+}/Er^{3+}$ Microstructures with Morphology- and Size-Dependent Upconversion Luminescence, Ceram. Int. 41 (2015) 7411–7420.

[34] Rasband, W.S., ImageJ, U. S. National Institutes of Health, Bethesda, Maryland, USA, http://imagej.nih.gov/ij/, 1997-2016.

[35] H.P. Klug, L.E. Alexander in X-ray Powder Diffraction Procedures, Wiley, New York, NY USA, 1959, p. 491.

[36] M.T. Berry, P.S. May, Disputed Mechanism for Nir-to-Red Upconversion Luminescence in $NaYF_4:Yb^{3+},Er^{3+}$, J. Phys. Chem. A. 119 (2015) 9805–9811.

[37] B.J. Selby, T.I. Quickenden and C.G. Freeman, The Fitting of Luminescence Rises and Decays, Kinet. Catal. 44 (2003) 5–15.

[38] H.F. Brito, J. Hölsä, T. Laamanen, T. Laihinen, M. Lastusaari, L.C.V. Rodrigues, L. Pihlgren, T. Soukka, Rare Earth Distribution in $NaRF_4$: Effect on Up-Conversion Intensity, *Powder Diffr.* 28 (2013) S41–S50.

[39] S.F. Lim, W.S. Ryu and R.H. Austin, Particle Size Dependence of the Dynamic Photophysical Properties of $NaYF_4$:Yb,Er Nanocrystals, Opt. Express 18 (2010) 2309–2316.

FIGURE CAPTIONS

Figure 1. Schematic presentation of the synthesis protocol for obtaining uniform-sized hexagonal $NaRF_4$ nanoparticles.

Figure 2. Energy transfer up-conversion mechanism of the Yb^{3+}/Er^{3+} pair [35]. ETU stands for energy transfer up-conversion and BET for back energy transfer.

Figure 3. X-ray powder diffraction patterns with the hexagonal and cubic $NaRF_4$ reference patterns [20] (top) and TEM-images of the $NaYF_4:Yb^{3+},Er^{3+}$ nanomaterials prepared with an argon flow of 1, 2 and 3 $dm^3\ h^{-1}$ (bottom). The scale bar represents 200 nm.

Figure 4. X-ray powder diffraction patterns with the hexagonal $NaRF_4$ reference pattern [20] (top) and TEM-images of the $NaYF_4:Yb^{3+},Er^{3+}$ nanomaterials prepared with a cooling time of 15 and 30 min (bottom). The scale bar represents 200 nm.

Figure 5. Effect of crystallite size on the green (top) and red (bottom) up-conversion luminescence intensities with visual fit. Abbreviations A1, 2, and 3 correspond to Argon flow of 1, 2 and 3 $dm^3\ h^{-1}$, C15 and 30 to cooling rate of 15 and 30 min, and S125, 200, 375, 500, and 625 to stirring rate of 125, 200, 375, 500, and 600, respectively.

Figure 6. Effect of crystallite size on the green (top) and red (bottom) up-conversion luminescence rise times with visual fit. For abbreviations see caption for Fig. 5.

Figure 7. Correlation between the rise:decay time and red:green emission intensity ratios with visual fit. Squares and circles represent green and red luminescence, respectively. For abbreviations see caption for Fig. 5. Data for the cubic material (A1) is not included.

Figure 8. Correlation between red (circles) and green (squares) up-conversion emission intensity and Er:Yb weight ratio. For abbreviations see caption for Fig. 5.

Figure 9. Red up-conversion luminescence intensity for selected $NaYF_4$:Yb^{3+},Er^{3+} nanomaterials (unchanged reaction parameters: argon flow rate 2 dm^3 h^{-1}, cooling time 30 min and stirring rate 375 rpm) as a function of the excitation power density.

Figure 10. Schematic presentation of the synthesis protocol and the factors affecting its outcomes.

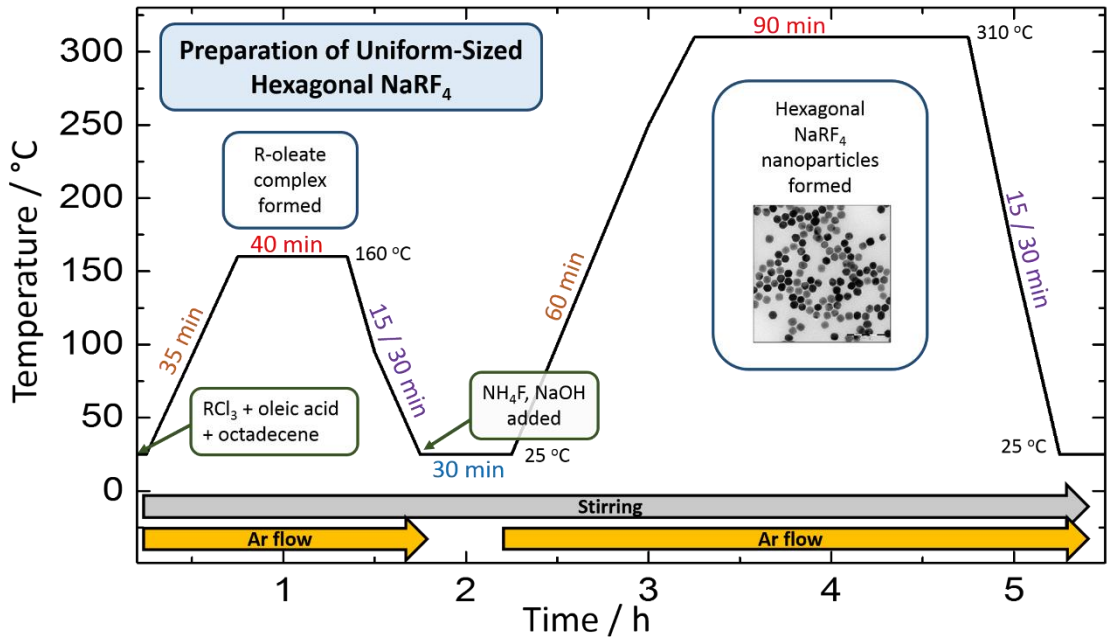

Figure 1. Schematic presentation of the synthesis protocol for obtaining uniform-sized hexagonal $NaRF_4$ nanoparticles.

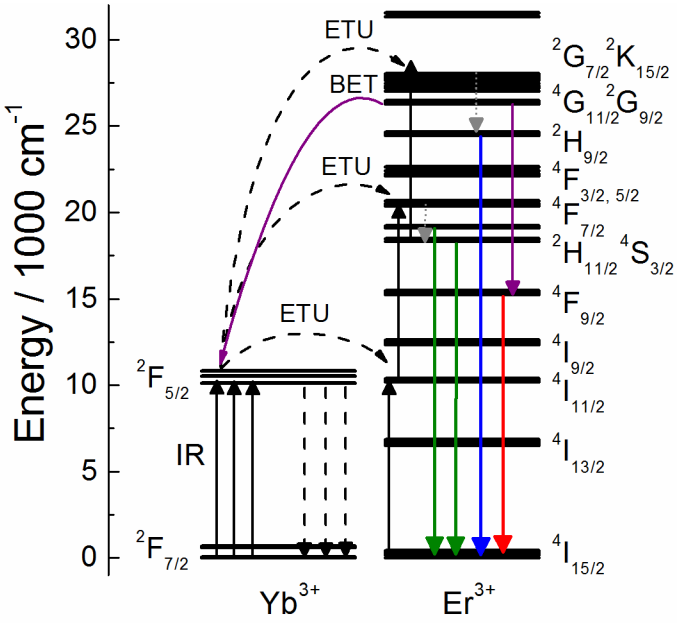

Figure 2. Energy transfer up-conversion mechanism of the Yb^{3+}/Er^{3+} pair [35]. ETU stands for energy transfer up-conversion and BET for back energy transfer.

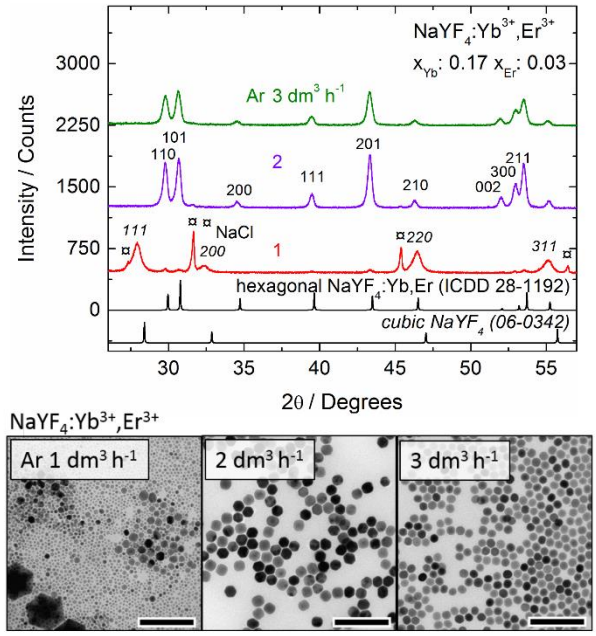

523

524 Figure 3. X-ray powder diffraction patterns with the hexagonal and cubic $NaRF_4$

525 reference patterns [20] (top) and TEM-images of the $NaYF_4:Yb^{3+},Er^{3+}$ nanomaterials

526 prepared with an argon flow of 1, 2 and 3 $dm^3\ h^{-1}$ (bottom). The scale bar represents

527 200 nm.

528

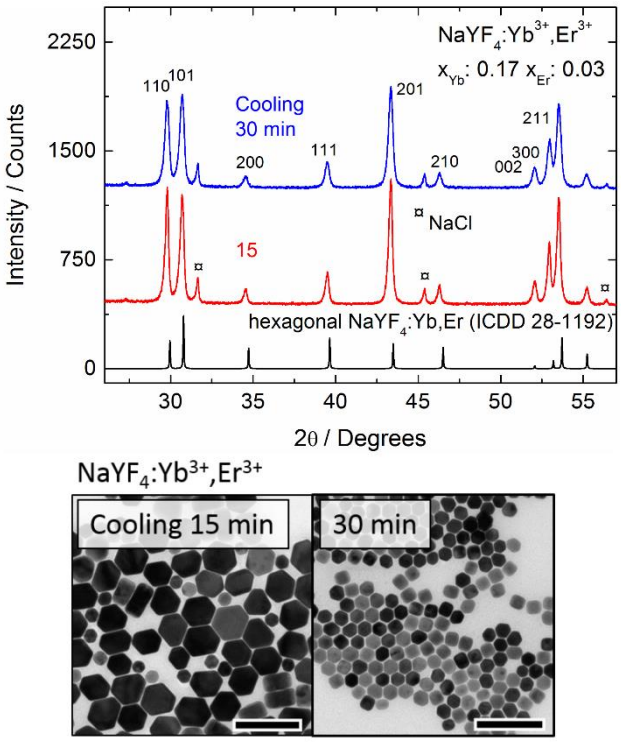

Figure 4. X-ray powder diffraction patterns with the hexagonal $NaRF_4$ reference pattern [20] (top) and TEM-images of the $NaYF_4:Yb^{3+},Er^{3+}$ nanomaterials prepared with a cooling time of 15 and 30 min (bottom). The scale bar represents 200 nm.

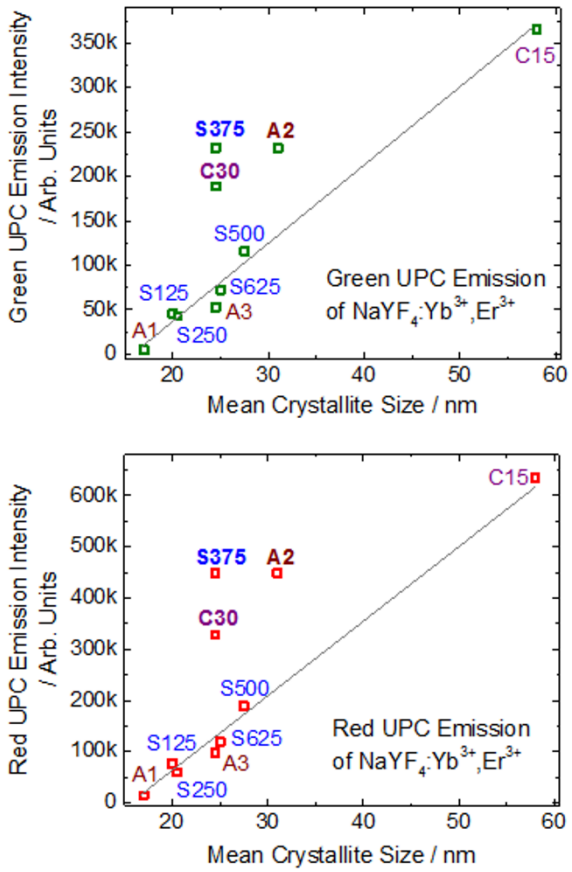

Figure 5. Effect of crystallite size on the green (top) and red (bottom) up-conversion luminescence intensities with visual fit. Abbreviations A1, 2, and 3 correspond to Argon flow of 1, 2 and 3 $dm^3\ h^{-1}$, C15 and 30 to cooling rate of 15 and 30 min, and S125, 200, 375, 500, and 625 to stirring rate of 125, 200, 375, 500, and 600, respectively.

542

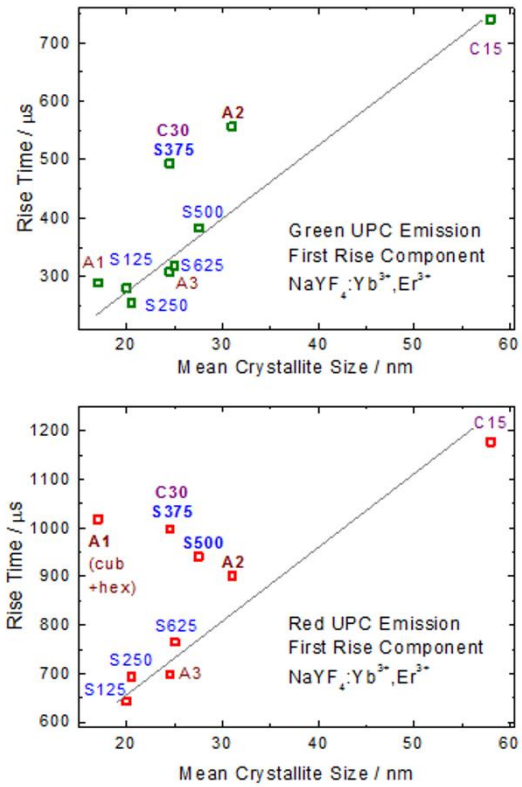

543

544 Figure 6. Effect of crystallite size on the green (top) and red (bottom) up-conversion

545 luminescence rise times with visual fit. For abbreviations see caption for Fig. 5.

546

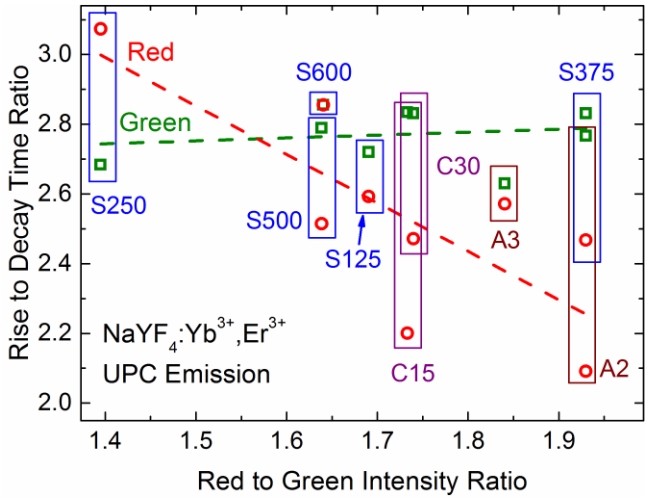

Figure 7. Correlation between the rise:decay time and red:green emission intensity ratios with visual fit. Squares and circles represent green and red luminescence, respectively. For abbreviations see caption for Fig. 5. Data for the cubic material (A1) is not included.

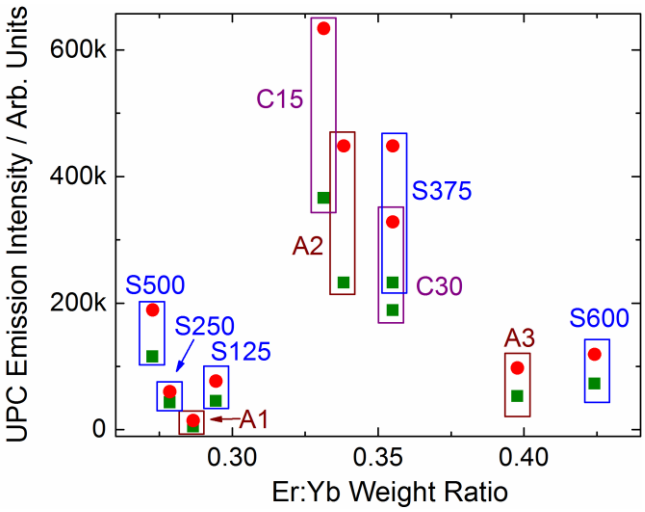

Figure 8. Correlation between red (circles) and green (squares) up-conversion emission intensity and Er:Yb weight ratio. For abbreviations see caption for Fig. 5.

559

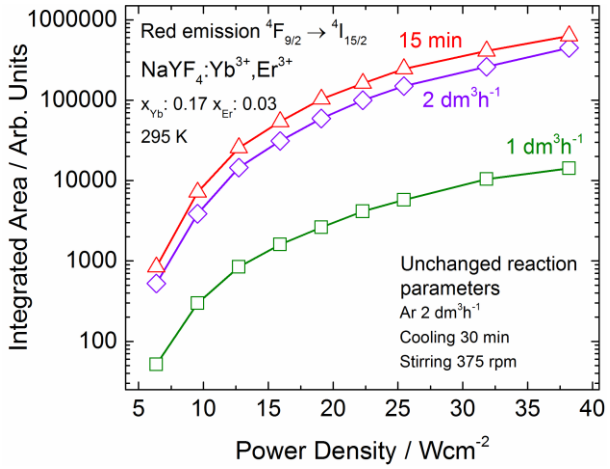

560

561 Figure 9. Red up-conversion luminescence intensity for selected $NaYF_4:Yb^{3+},Er^{3+}$

562 nanomaterials (unchanged reaction parameters: argon flow rate 2 dm^3 h^{-1}, cooling

563 time 30 min and stirring rate 375 rpm) as a function of the excitation power density.

564

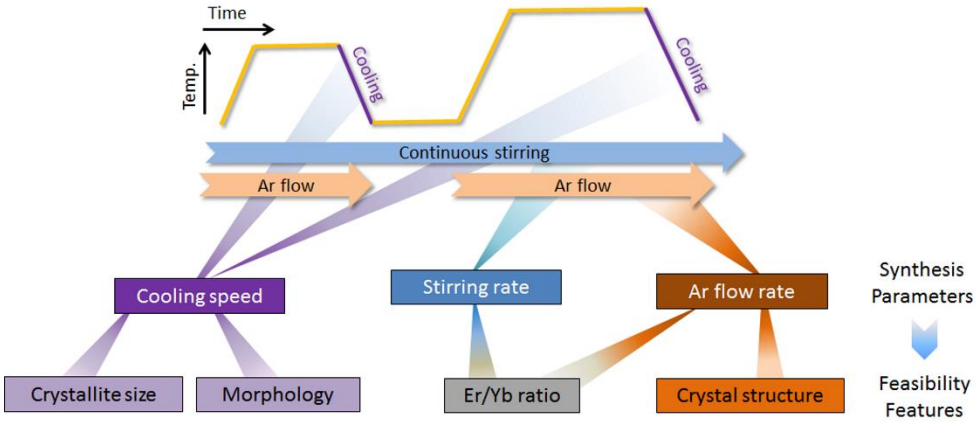

Figure 10. Schematic presentation of the synthesis protocol and the factors affecting its outcomes.